Journal of Medical Imaging

MedicalImaging.SPIEDigitalLibrary.org

INSIDE in-beam positron emission tomography system for particle range monitoring in hadrontherapy

Maria Giuseppina Bisogni
Andrea Attili
Giuseppe Battistoni
Nicola Belcari
Niccolo' Camarlinghi
Piergiorgio Cerello
Silvia Coli
Alberto Del Guerra
Alfredo Ferrari
Veronica Ferrero
Elisa Fiorina
Giuseppe Giraudo
Eleftheria Kostara
Matteo Morrocchi
Francesco Pennazio
Cristiana Peroni
Maria Antonietta Piliero
Giovanni Pirrone
Angelo Rivetti
Manuel D. Rolo
Valeria Rosso
Paola Sala
Giancarlo Sportelli
Richard Wheadon

Maria Giuseppina Bisogni, Andrea Attili, Giuseppe Battistoni, Nicola Belcari, Niccolo' Camarlinghi, Piergiorgio Cerello, Silvia Coli, Alberto Del Guerra, Alfredo Ferrari, Veronica Ferrero, Elisa Fiorina, Giuseppe Giraudo, Eleftheria Kostara, Matteo Morrocchi, Francesco Pennazio, Cristiana Peroni, Maria Antonietta Piliero, Giovanni Pirrone, Angelo Rivetti, Manuel D. Rolo, Valeria Rosso, Paola Sala, Giancarlo Sportelli, Richard Wheadon, "INSIDE in-beam positron emission tomography system for particle range monitoring in hadrontherapy," *J. Med. Imag.* **4**(1), 011005 (2017), doi: 10.1117/1.JMI.4.1.011005.

SPIE.

INSIDE in-beam positron emission tomography system for particle range monitoring in hadrontherapy

Maria Giuseppina Bisogni,[a,b,*] Andrea Attili,[c,d] Giuseppe Battistoni,[e] Nicola Belcari,[a,b] Niccolo' Camarlinghi,[a,b] Piergiorgio Cerello,[d] Silvia Coli,[d] Alberto Del Guerra,[a,b] Alfredo Ferrari,[f] Veronica Ferrero,[c,d] Elisa Fiorina,[d] Giuseppe Giraudo,[d] Eleftheria Kostara,[b] Matteo Morrocchi,[a,b] Francesco Pennazio,[d] Cristiana Peroni,[c,d] Maria Antonietta Piliero,[a,b] Giovanni Pirrone,[a,b] Angelo Rivetti,[d] Manuel D. Rolo,[d] Valeria Rosso,[a,b] Paola Sala,[e] Giancarlo Sportelli,[a,b] and Richard Wheadon[d]

[a]University of Pisa, Department of Physics, Largo B. Pontecorvo 3, 56127 Pisa, Italy
[b]Istituto Nazionale Fisica Nucleare INFN, Sezione di Pisa, Largo B. Pontecorvo 3, 56127 Pisa, Italy
[c]University of Torino, Department of Physics, Via Pietro Giuria 1, 10125, Torino, Italy
[d]Istituto Nazionale Fisica Nucleare INFN, Sezione di Torino, Via Pietro Giuria 1, 10125, Torino, Italy
[e]Istituto Nazionale Fisica Nucleare INFN, Sezione di Milano, Via Celoria 16, 20133, Milano, Italy
[f]Organisation Européenne pour la Recherche Nucléaire CERN, CH-1211, Geneva 23, Switzerland

Abstract. The quality assurance of particle therapy treatment is a fundamental issue that can be addressed by developing reliable monitoring techniques and indicators of the treatment plan correctness. Among the available imaging techniques, positron emission tomography (PET) has long been investigated and then clinically applied to proton and carbon beams. In 2013, the Innovative Solutions for Dosimetry in Hadrontherapy (INSIDE) collaboration proposed an innovative bimodal imaging concept that combines an in-beam PET scanner with a tracking system for charged particle imaging. This paper presents the general architecture of the INSIDE project but focuses on the in-beam PET scanner that has been designed to reconstruct the particles range with millimetric resolution within a fraction of the dose delivered in a treatment of head and neck tumors. The in-beam PET scanner has been recently installed at the Italian National Center of Oncologic Hadrontherapy (CNAO) in Pavia, Italy, and the commissioning phase has just started. The results of the first beam test with clinical proton beams on phantoms clearly show the capability of the in-beam PET to operate during the irradiation delivery and to reconstruct on-line the beam-induced activity map. The accuracy in the activity distal fall-off determination is millimetric for therapeutic doses. [DOI: 10.1117/1.JMI.4.1.011005]

Keywords: hadrontherapy; particle range verification; positron emission tomography.

Paper 16155SSR received Jul. 29, 2016; accepted for publication Nov. 15, 2016; published online Dec. 2, 2016.

1 Introduction

Hadrontherapy is a cancer therapy performed with ions (mostly protons and carbon ions) for the treatment of solid and radioresistant tumors located in the vicinity of critical organs.[1,2] Its effectiveness derives mainly from the characteristic deposition of the dose that can be determined with submillimeter accuracy by calculating the position of the so-called Bragg peak (BP), that is the region with maximum dose delivered to the tissues. However, the extreme precision of this therapy may be impaired if the charged particles' actual path (hereinafter called "dose range") is significantly different from the expected value calculated by the treatment planning system. Range uncertainties can be caused by errors in the stopping power calibration from the planning computed tomography (CT), physiological changes in the patient morphology, or errors in positioning the patient in the treatment room.[3] In clinical practice, range uncertainties are taken into account, allowing large safety margins (up to 3% +3 mm in proton therapy) around the tumor and avoiding the beam directions along which the BP would be too close to critical organs.[4] In order to fully exploit the advantages of ion therapy, an *in-vivo* monitoring of the particle range is highly recommended.

The most used noninvasive method to monitor *in-vivo* the range of the charged particles is based on the measurement of the $\beta+$ activity induced by the interaction of the therapeutic beam with the patient tissue by means of positron emission tomography (PET).[5] Therapeutic ions can produce target fragments, such as ^{11}C, ^{15}O, and ^{38}K (among the most abundant) from ^{12}C, ^{16}O and ^{40}Ca nuclei, resulting in activation along the beam path with a fall-off (protons) or a small activity tail (heavier ions) a few millimeters before the BP.[6] Moreover, primary ion beams with charge $Z \geq 5$ can undergo projectile fragmentation yielding additional $\beta+$ emitting isotopes. Determining the dose range from the activity measurement is not straightforward since dose and production of radioactive nuclides depend in a different way on ion species, energies, and tissue composition. The problem is further complicated in real clinical situations by low-induced signal levels and physiological washout. In fact, the $\beta+$ activity formed in nuclear interactions (maximum a few kBq/ml/Gy) is almost two orders of magnitude below the typical activity concentrations in diagnostic nuclear medicine (ca. 50 kBq/ml in hot spots). In addition, the induced activity is rapidly lost due to the physical decay of the sources (the main isotopes produced, ^{15}O and ^{11}C, have half-lives of 2 and 20 min, respectively) and physiological washout, with produced isotopes binding to different molecules and

*Address all correspondence to: Maria Giuseppina Bisogni, E-mail: giuseppina.bisogni@pi.infn.it

2329-4302/2016/$25.00

undergoing functional pathways, such as perfusion and diffusion. Based on such considerations, the primary goal of PET monitoring so far is the beam range assessment that is usually performed by comparing the measured PET data with Monte Carlo data obtained starting from the patient treatment plan simulation.[7] PET imaging for *in-vivo* range verification of ion beams is performed with commercial scanners placed in an adjacent room to the treatment (off-line PET) or in the immediate vicinity of the patient (in-room PET).[8] Alternatively, ad-hoc systems[9] are moved to the treatment site after the end of the irradiation (*in-situ* PET). However, PET scanners integrated in the treatment gantry or nozzle and operating during the delivery of the beam (in-beam PET) allows achievement of higher sensitivities in the measurement of the low-induced activity levels.[10] The in-beam PET systems configuration greatly depends on the ion accelerator facility. Cyclotron machines (the vast majority for proton therapy) produce continuous beams. Due to the high background during the continuous beam delivery and the passive beam shaping, the PET signal is usually acquired after the end of the irradiation as in the case of the in-beam PET system integrated in the proton gantry of the National Cancer Center Hospital in Kashiwa, Japan.[11] Synchrotron machines are used to accelerate both protons and light ions, with a beam delivery time structure characterized by an extraction phase (spill) and a pause between two spills when the beam acceleration phase takes place (interspill). In such facilities, in-beam PET systems have been previously developed and operated in the clinic during the pause of the spills or immediately after the irradiation, but their functioning was hampered during the actual beam delivery due to the high background radiation consisting of high energy prompt photons and neutrons.[12–14] At the GSI Helmholtzzentrum für Schwerionenforschung synchrotron therapeutic beam line (Darmstadt, Germany), more than 400 patients, treated with protons and ^{12}C ions, were imaged with an in-beam double head PET camera integrated in the treatment unit between 1999 and 2008.[15] To avoid the beam-induced background during the spills, the PET acquisitions were allowed during the pauses between two spills (interspill) and for 40 s after the irradiation (after-treatment).

Recently, substantial improvements in PET technology enabled the construction of new in-beam PET prototypes based on fast acquisition electronics. One such system was able to operate during the beam delivery in a cyclotron-based facility (the INFN-LNS CATANA protontherapy facility, in Catania, Italy)[16] with low energy proton beams (up to 68 MeV). However, the performance of the same system tested at the National Center of Oncologic Hadrontherapy (CNAO,[17] Pavia, Italy) synchrotron facility was greatly reduced during the in-spill phases of the irradiation session.[18] In fact, the electronics was paralyzed by the high count rate induced by the prompt radiation produced by the nuclear reactions of the primary beams with the traversed material. Despite similar beam intensities, the CNAO beam energies were higher than those at CATANA, and thus more prompt radiation was produced per beam particle. Furthermore, due to the pulsed structure of the CNAO beam, the particles' instantaneous rate was an order of magnitude higher than that at CATANA.

The correct acquisition of both the in-spill and interspill signals would allow extraction of the maximum information over the whole irradiation cycle. This is even more important for synchrotrons with improved duty cycles, where the interspill interval is reduced to shorten the treatment duration. On the other hand, in-spill data may be corrupted by random coincidences arising from prompt radiation following nuclear reactions of the beam with the tissue. The random events cannot be suppressed by applying the conventional techniques used in PET like the delayed coincidence method or the single count-rate method,[19] since the random temporal distribution depends on the microstructure of the beam (i.e., it is not uniform). Random events can be removed by an anticoincidence with the microscopic beam pulse. Coincidence events detected with the PET scanner can be correlated with the radio frequency signal or with the signal of a fast particle detector placed in front of the target, and they can be either labeled for a-posteriori suppression or immediately discarded. These methods have been successfully tested with carbon ions at the GSI but never turned into clinical practice.[20]

In 2013, the Innovative Solutions for Dosimetry in Hadrontherapy (INSIDE) collaboration[21] proposed a similar approach to be implemented in a PET scanner operated during the treatment of head and neck tumors. The INSIDE in-beam PET scanner is based on fast pixelated scintillators coupled one-to-one to silicon photomultipliers (SiPMs), and the readout electronics, designed to cope with the count rate expected from synchrotron beams during the spill phase, provides the energy and the timestamp of each detected event for a time-resolved analysis of the acquired signals. The expected sensitivity and spatial resolution meet the requirement to reconstruct the induced activity with millimetric accuracy within a fraction of the therapeutic plan (typically 2 Gy administered in less than 5 min for a head–neck treatment fraction at CNAO).

In case of ^{12}C therapeutic beams, the information provided by the PET system can be improved with the knowledge of the beam profile within the patient, which can be measured by tracking secondary particles (mainly protons) promptly emitted from the projectile fragmentation.[22] The secondary emission point distribution can be reconstructed by backpointing the track of the charged particle to the beam path.[23] In this respect, INSIDE represents an innovative bimodal imaging concept where the simultaneous detection of annihilation photons and prompt charged particles provides a robust range verification method in the treatment of head and neck tumors with protons and carbon ions. The INSIDE system is composed of an in-beam PET scanner and a charged particle tracking system, also called dose profiler. The mechanical structure has been designed to accommodate the system in the CNAO treatment room,[24] the only Italian therapeutic facility treating with proton and carbon ion beams. The ultimate objective of the project is the development of a quality control procedure based on the comparison between the expected signal and the signal measured by the two detection systems. This objective is pursued through the development of Monte Carlo codes for the prediction of $\beta+$ activation and of charged particles production.[25,26] An integral part of the procedure is the development and application of PET images and charged particles track reconstruction algorithms.

The in-beam PET part of the INSIDE project was recently completed with the installation of the PET system at CNAO, where it is currently in the commissioning phase. The dose profiler is being assembled, and its integration in the INSIDE system at CNAO is scheduled within the year. Therefore, the description of the profiler will be limited to its general design. This paper focuses on the INSIDE in-beam PET system design and construction and reports the first results achieved in view of

its clinical validation. Following this introduction, Sec. 2 contains the INSIDE system description, in particular the PET system, then the experimental set-up adopted for the tests and the data processing and analysis methods. In Sec. 3, we present the experimental results in terms of imaging capability and the comparison with the simulations.

2 Material and Methods

2.1 *INSIDE Bimodal System*

The bimodal INSIDE imaging system consists of an in-beam PET scanner made of two opposite planar heads and a dose profiler for charged particles tracking. The two detectors are integrated into a support structure whose geometry has been optimized to fit the nozzle of the CNAO treatment room. The mechanical structure is constituted by two subassemblies that form a homogeneous group: a base cart, with the horizontal handling and leveling devices and the positioning of the dose profiler holder, and the vertical shoulder that supports the mechanical positioning of the PET heads. The cart and shoulder are made of aluminum alloy profiles. The weight of the global system, comprised of the PET scanner and the dose profiler, is about 300 kg, and its size is 110 cm (L) × 110 cm (W) × 160 cm (H).

The detectors are maintained at the temperature of 18°C by means of a water cooling hydraulic circuit fed by a chiller whose operating flow rate is about 8 l/ min.

Figure 1 shows the solid model of the system in the measurement position with the two heads PET system and the dose profiler. The system can be easily placed in the measurement position with the help of markers on the PET heads that are aligned with the positioning lasers of the treatment room. The achieved accuracy is below 1 mm. The default working distance between the PET heads is 50 cm, symmetrical with respect to the isocenter of the treatment room. The double PET head geometry is renowned for being not optimal for the lack of tomographic capability, limited angle sampling, and reduced solid angle coverage. But, for in-beam PET, this is the standard approach since it allows it to stay as close as possible to the patient, without hampering the patient-bed motion and the particle beam path.

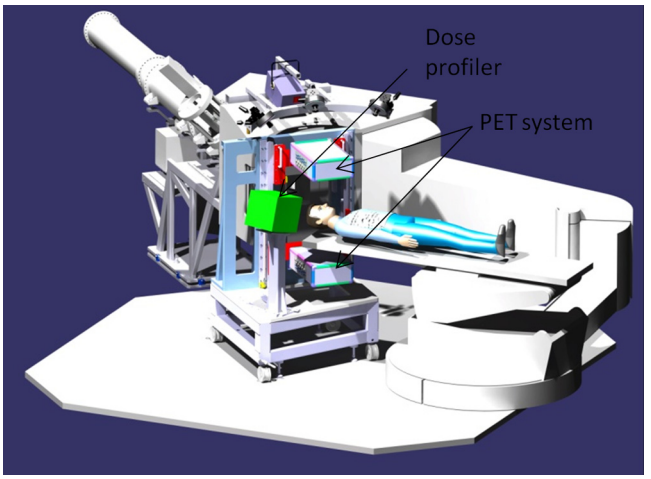

Fig. 1 Solid model of the INSIDE system in the measurement position, with the two heads PET subsystem and the dose profiler. The beam line and nozzle of the CNAO treatment room are shown in gray.

The dose profiler is placed instead on a column of 100 cm height, inclined 60 deg with respect to the direction of the horizontal beam to maximize the secondary particles flux crossing the dose profiler. The profiler consists of a tracker followed by a calorimeter. The tracker is made of six layers of scintillating fibers in orthogonal views, which allow the reconstruction of the track and the point of origin of protons exiting from the patient with about 100% efficiency. The 19.2 cm × 19.2 cm tracker planes are made of square (500 μm × 500 μm) multicladding fibers from Saint-Gobain, read with SiPMs. The calorimeter, used for the measurement of the energy of the charged particles detected in each event, is made of 4 × 4 lutetium–yttrium oxyorthosilicate (LYSO) crystal pixels matrices (64 pixels of 3 mm × 3 mm × 20 mm each) read by the multianode PMT H8600.[27] The PMTs have been used instead of SiPMs since they allow achieving, with a lower number of channels, the spatial resolution necessary to avoid the erroneous association of energy releases in case of a pile-up in the calorimeter. Furthermore, the electronics read-out system was already available from a previous development.

2.2 *INSIDE In-Beam Positron Emission Tomography*

2.2.1 *Detection modules and positron emission tomography heads*

The PET detector is based on the latest technology of solid-state photodetectors (SiPM) with high granularity (3 mm pitch) and one-to-one coupling to lutetium fine silicate (LFS) pixelated scintillating crystals. LFS is particularly suitable for PET applications since it is comparable to lutetium oxyorthosilicate and LYSO (the most used scintillators in PET) for density (7.35 g/cm^3) and light yield (80% with respect to NaI:Tl) but has improved time performances (its ~33-ns decay constant makes it the fastest one among lutetium-based silicates).[28]

SiPMs are solid-state photodetectors made of arrays of avalanche photodiodes operated in Geiger mode:[29,30] with respect to conventional photomultiplier tubes (PMTs), they are faster and insensitive to magnetic fields. With respect to standard avalanche photodiodes operated in linear mode, they produce a more stable output, thus providing better energy resolution. Modern PET systems including time-of-flight (ToF) capability[31] or integrated with magnetic resonance imaging scanners[32] are based upon this technology.[33,34]

An advantage of SiPMs over PMTs is their compactness: SiPMs can be arranged in arrays of small pixels that can be read out independently or in small parallel subsets. This allows for a strong reduction in the dead-time per unit area, thus enabling the read-out and processing of event rates typical of operations during the treatment delivery [order of 10^7 counts per second (cps) in a 10 × 25 cm^2 area].[35]

A detection module of the INSIDE in-beam PET system consists of a matrix of 16 × 16 LSF crystals, 3 × 3 × 20 mm^3 each, optically coupled to SiPMs. The module area is 51.2 × 51.2 mm^2. Ten detection modules are disposed in a 2 × 5 array, with a 3.3-mm gap in between. The array covers an area of 112 mm (transaxial) × 264 mm (axial, along the direction of the beam). The total number of detector channels in one PET head is 2560.

The 2 × 2560 detector channels are processed by front end (FE) integrated electronics and a highly parallelized data acquisition (DAQ) system based on field programmable gate array

(FPGA). Figure 2 shows a conceptual block diagram of the PET system comprehending the SiPM matrices, the FE boards, and the DAQ components.

The TOFPET[36] application-specific integrated circuit (ASIC) (developed in the framework of the European FP7 project ENDOTOFPET[37]) was selected for the read-out of the SiPMs outputs. The ASIC, developed in IBM CMOS 130 nm technology, features 64 channels capable of supporting an input event rate up to 100 kHz. The ASIC outputs the energy and the arrival time (also called the time stamp) of the event encoded through a time-to-digital converter with a resolution of 50 ps. The energy information is obtained with the time over threshold (TOT) method. A threshold is set on both the rising edge and the falling edge of the pulse generated in the analog stage of the FE channel. A first time stamp is assigned when the pulse crosses the threshold on the rising edge, and a second time stamp is assigned when the pulse crosses the threshold on the falling edge. The duration of the pulse is given by the difference between the two time stamps and provides a measure of the energy released in the detector. Using two threshold levels, one can also precisely measure the leading edge of the event while suppressing the dark counts from the SiPM.

A custom-made FE board hosts the four TOFPETs required for the readout of one detection module.

A box made of aluminum alloy contains the array of 10 detection modules and the FE boards. The box is connected to the positioning stage through a flange. The detection modules are fixed to the box by means of a support plate of plastic material (epoxy glass). The electronic read-out, which dissipates ~60 W in total, is fixed to a cooling plate (or heat sink) and thermally connected to it through electrically insulating thermal pads. The cooling plate, constructed by fusion of an aluminum alloy, incorporates a steel tube, bent in serpentine, in which water circulates at the temperature of 18°C, with a $Q = 2$ l/ min flow rate. The value of the input temperature can be varied as a function of the dew point in the treatment room.

Figure 3 shows the components of a PET head. Figure 3(a) shows the crystal matrix on the left, the SiPM matrix in the center, and the hybrid rigid-flex circuit on the right. This circuit is needed to bring power supplies to the photodetectors and the current signals to the inputs of FE integrated circuits. The three assembled elements are enclosed in a 0.5-mm thick aluminum case to form a detection module. The modules were developed by Hamamatsu Photonics[27] [model S12642-1616-3577(X), SiPMs microcell size 50 μm]. Figure 3(b) shows the 10 detection modules assembled in the 2×5 array. Figure 3(c) shows the inside of the aluminum box with details of the detection modules placement (on the back side, not visible), the FE boards attached to the cooling plate (on the sides), and the water cooling (red and transparent pipes).

The PET system is managed by dedicated LabView software that controls the chiller, the power supply, and the electronics, and allows loading the calibration files and changing the acquisition parameters of the FE circuits.

2.2.2 *Data acquisition and processing*

The signals from the FE ASICs are processed by 20 Xilinx SP605 FPGA boards (named TX boards) that can also filter the events by selecting those falling within an adjustable energy window around the 511-keV photopeak.

The event selection is based on the energy calibration of all the PET channels. The TOT spectra of a $\beta+$ source (typically ^{22}Na or a ^{68}Ge) are acquired for each channel (the average energy resolution was 13%), and the maximum of counts corresponding to the 511-keV photopeak is identified with an automated software procedure. A symmetric window of fixed width (typically ± 3 sigma) and centered around the photopeak is then applied to all channels. The intervals of TOT values found for each channel are written in a calibration file that is then loaded on the TX FPGAs. The filtering algorithm, implemented in the FPGA firmware, selects the events falling in the energy window according to the values found in the calibration file.

The TX boards transmit the decoded and filtered data to the DAQ server (32 cores HT, 128 GB ram) by means of a 24-port switch through 2 Gbit/s Ethernet cables. A dedicated and optimized multithreading C/C++ software based on BOOST libraries applies data sorting and coincidence finding and writes time-tagged coincidence data real-time. The coincidence time window applied is 2 ns, that is wide enough to cover a PET nuclide distribution of ± 15 cm from the center of the

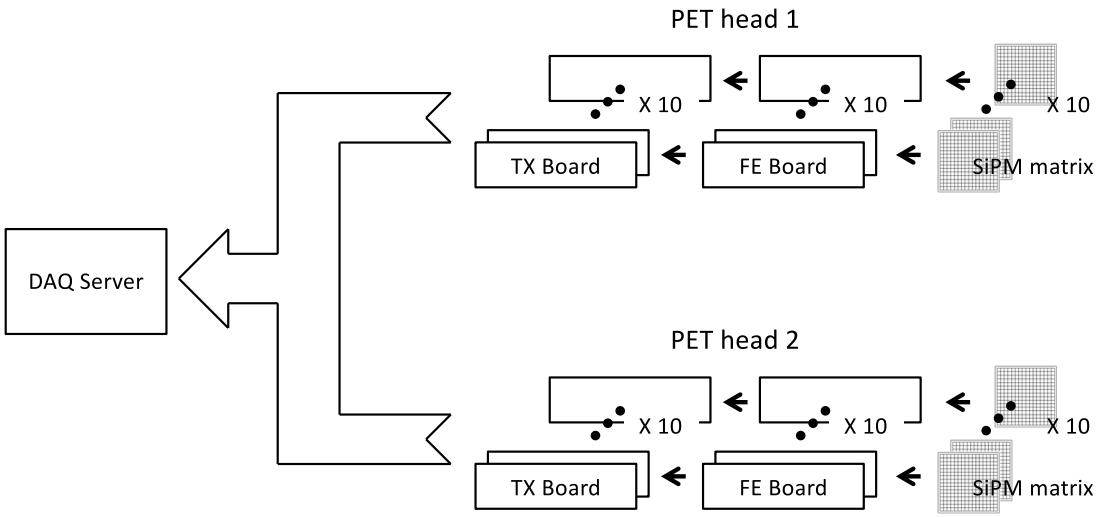

Fig. 2 Conceptual block diagram of the PET system comprehending the SiPM matrices, the FE boards, and the DAQ components.

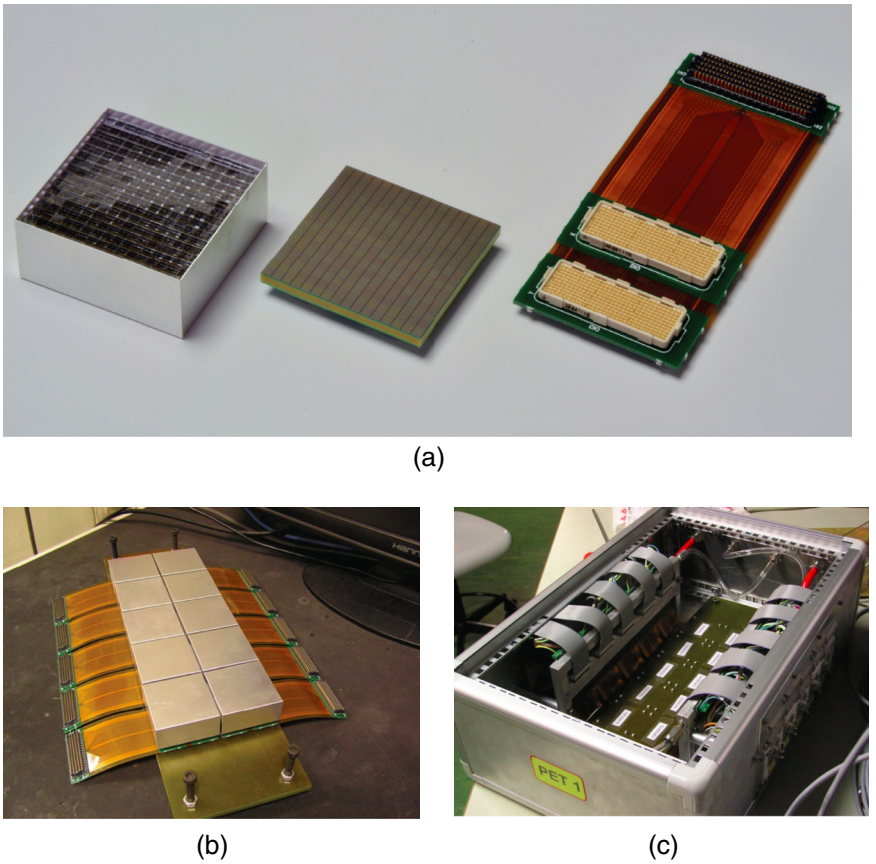

Fig. 3 (a) The crystal matrix (left), the SiPM matrix (center), and the hybrid rigid-flex circuit (right; courtesy of Hamamatsu Photonics[27]). (b) 10 detection modules assembled in the 2×5 array. (c) Inside of the PET box with details of the detection modules (on the back), FE boards (on the sides), and water cooling.

field-of-view (FoV); it is also consistent with a measured coincidence time resolution (CTR) of 450 ps (sigma). With the beam set-up described in Sec. 2.3, the system correctly acquired and analyzed data up to 2×10^7 cps in-spill single event rate in the photopeak window.

A tunable subset of the single event data and all the coincidences are forwarded through user datagram protocol from the DAQ to a conventional quad-core i5 PC, where a graphical user interface controls C/C++ software based on ROOT/BOOST libraries. The software performs the calibrations on the system (energy and time delay calibrations), monitors on-line its performance (CTR measurements), and writes line-of-response (LoR) files in list mode during DAQ.

The single events online monitoring is also used to separate the coincidences in two groups: in-spill and interspill data. The separation is operated by measuring the event rate and comparing it with a threshold.

A maximum likelihood estimation maximization (MLEM) iterative algorithm[38] is used for the on-line or off-line three-dimensional (3-D) PET image reconstruction.[39] Five iterations were used to reconstruct the images acquired in this work, with an execution time of ~1 s on a 3.4 GHz Intel Core i7-3770 CPU. The FoV of the reconstructed image is $224 \times 112 \times 264$ mm^3, with a $1.6 \times 1.6 \times 1.6$ mm^3 voxel size.

The real-time reconstruction capability provides on-the-fly imaging of the activity map during the beam delivery (provided there is enough statistics), thus enabling the perspective of almost real-time range assessment with the possibility of providing a feedback to the beam delivery system (e.g., an emergency beam stop).

2.3 *Experimental Set-Up*

The INSIDE in-beam PET system was recently installed at CNAO and preliminary tests were performed with different irradiation settings. Figure 4 shows the in-beam PET system fully assembled and installed in one of the CNAO treatment rooms.

Beams of protons on polymethyl methacrylate (PMMA) phantoms, with and without air cavities, and anthropomorphic plastic phantoms were used to test the system performance in controlled configurations.

Figure 5 shows the layout (not to scale) of the set-up adopted for the PMMA phantoms [Fig. 5(a)] and a picture of the set-up with the anthropomorphic phantom [Fig. 5(b)] that reproduces a typical clinical treatment setting. The INSIDE PET top head is visible in the upper part of the picture. The anthropomorphic phantom used was the ALDERSON-RANDO[40] made from tissue equivalent material modeled around a skeletal component, divided into 2.5 cm cross-sections and equipped with suitable housings for the dosimeters, in correspondence to the various anatomical landmarks.

The CNAO synchrotron[41] typical beam time structure is a sequence of 1 s beam on (in-spill) followed by 3 to 4 s beam-off (interspill). The beam intensity was about 2×10^9 protons per spill. At CNAO, the beam is distributed into the target by means of an active beam delivery system with the target

Fig. 4 The INSIDE in-beam PET system fully assembled and installed in one of the CNAO treatment rooms.

subdivided in isorange slices or energy layers. The beam energy is set so that the BP is in the first slice. A pencil beam of a given energy is displaced by two scanning magnets to paint a slice in order to deliver the planned dose to every spot. When the slice is finished, the beam is stopped and a new beam is accelerated to a higher energy, corresponding to the second slice. The process is repeated until the treatment plan is completed. For our measurements, we used single energy pencil beams, single energy layers, and real (i.e., actually delivered to patients in clinical treatments) treatment plans. The beams energies (from 74 to 135 MeV) and doses (order of 1 to 2 Gy) were typical of treatments in the head–neck district.

The aim of the tests with the PMMA phantoms was to perform a first evaluation of the system performances by separately analyzing the datasets acquired during the in-spill and interspill phases of the irradiation session.

A first set of measurements was performed on a $5 \times 5 \times 14$ cm^3 homogenous PMMA phantom irradiated with a proton pencil beam of 124 MeV (BP at a depth of 11.1 cm in water). The center of the phantom is coincident with the beam isocenter. The total number of protons was 2×10^{10} (delivered in 17 spills for a total treatment time of 85 s) and the dose was 1 Gy.

A second set of measurements was performed on a homogeneous $4.9 \times 4.9 \times 14$ cm^3 PMMA phantom (named phantom A) and on a $4.9 \times 4.9 \times 12.9$ cm^3 PMMA phantom (named phantom B) with a $4.9 \times 4.9 \times 1$ cm^3 air hole after 4.9 cm along the beam axis. The two phantoms were irradiated with two subsequent proton energy layers of 75 (first layer) and 103.5 MeV (second layer), respectively.

The choice of such a configuration of the phantoms and the beams was motivated by the need to test the simulations (see Sec. 2.4) in easily reproducible conditions.

The two energy layers, being part of different treatment plans, were applied at different times. The corresponding BP positions in homogenous PMMA are located at $z = 4.02$ cm and $z = 7.06$ cm. Table 1 reports the acquisition time durations for the two irradiated phantoms. The acquisition times differ for the two phantoms due to the different delivery of the beam in the two irradiation settings. Nevertheless, the area of both layers was 3×3 cm^2 and the dose was 2 Gy for each layer and for each phantom.

Deviations from the expected range can arise from energy and tissue composition variations. This, in general, is reflected in a different length of the activity induced by the beam in the tissue (hereafter called activity range). In our acquisitions with the PMMA phantoms, the particle range has been measured in terms of activity range induced in both homogeneous and heterogeneous phantoms from primary beams of fixed and variable energies. The activity range was evaluated starting from the one-dimensional (1-D) profile defined as the voxel intensity along the beam direction (the z axis in our reference system) of the 3-D image slice passing through the isocenter and parallel to the PET heads. To reduce the statistical fluctuations, the profiles were obtained considering the integrated counts (for each slice

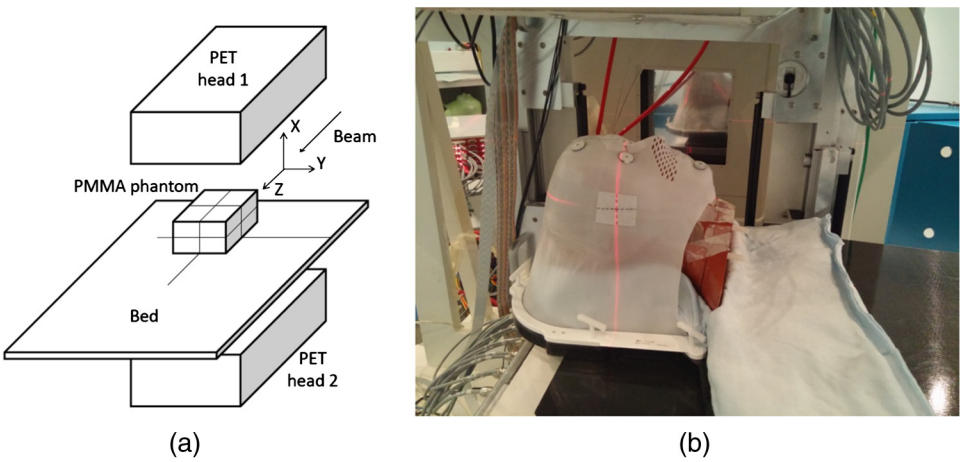

Fig. 5 (a) Lay-out (not to scale) of the set-up adopted for the PMMA phantoms and reference axis. (b) Set-up adopted for the anthropomorphic phantom acquisitions that reproduces a typical clinical treatment setting. The PET top head is visible in the upper part of the picture.

Table 1 Acquisition time durations for the two irradiated phantoms.

Phantom	First slice delivery duration (s)	Interslices time interval (s)	Second slice delivery duration (s)	After-treatment duration (s)	Total acquisition duration (s)
A	36	171	47	268	519
B	17	124	14	330	485

orthogonal to the beam direction) of a rectangular 24×8 voxels region of interest (ROI) surrounding the activated area.

The distal fall-off of the profiles was fitted with a sigmoidal function described by the following equation:

$$i = \frac{A - B}{1 + e^{\frac{z-d}{s}}} + B, \tag{1}$$

where A and B are related to the maximum and minimum values of the ROI counts i along the profile, respectively, s is the slope of the distal fall-off, and d is the inflection point coordinate along the z axis. A and B depend on the actual beam intensity, treatment duration, and data integration time, while d provides a measure of the activity range inside the phantom.

2.4 *In-Beam Positron Emission Tomography Simulations*

Since the procedure for range assessment is usually based on the comparison between the expected PET image and the one measured by the detection system, it requires the development of simulations or analytical models of the treatments plans on phantoms and patients and the modeling of the detection systems. Within the INSIDE project, this was carried out by implementing a Monte Carlo code based on FLUKA[42,43] for the description of the CNAO beam line and for the prediction of the induced $\beta+$ activity, the production of prompt photons and charged particles. The ultimate goal is to realize a semiautomated tool for range comparison between measured and reference (simulated or measured in previous sessions) distributions.

For the in-beam PET system, a two-step simulation technique was developed and implemented with a 70× reduction in computing time when compared to a full one-step simulation.[26] Basically, it consists in the production of the $\beta+$ isotopes map starting from the simulation of the beam with limited statistics (typically 1/100 of the actual amount of protons delivered). The isotope map is the input of the second step in which a full statistics simulation, including the detector and front-end electronics response, generates the emission time of all positrons and the LoR generated by the detection of their annihilation products. The simulation tool can import the information provided by the CNAO dose delivery system (DDS),[44] which regulates the delivery of the pencil beams, steered and held to the prescribed positions until the prescribed number of particles has been delivered. DDS provides as output a log file with the actual beams delivered as a function of time and it serves as input for the INSIDE simulation. More details can be found in Ref. 26, in which we report on the Monte Carlo validation on a previous experimental set-up comprehending a small-scale prototype of the INSIDE PET system and PMMA phantoms irradiated by monoenergetic pencil beams of 68 and 72 MeV.

Starting from these results, the code has been expanded to model the full-scale INSIDE PET system. In the simulations presented here, we have reproduced the same measurements set-up adopted for the PMMA phantoms A and B (see Sec. 2.3 for set-up geometry, materials compositions, beam energies, beam time structure, and after-treatment duration). The isotopes simulated are ^{11}C, ^{10}C, ^{15}O (among the most abundant), ^{14}O, ^{13}O, ^{13}N, ^{12}N, ^{9}C, ^{8}B, which together account for 99.98% of the isotopes produced in PMMA for the given beam settings. Physical processes other than $\beta+$ isotopes production and annihilations of positrons emitted from those isotopes decays were not taken into account. Therefore, the comparison between experimental data and simulation was limited to the interspill and after-treatment phases only.

The postprocessing and analysis were performed using the same parameters (i.e., same energy and time windows) and with the same procedures (analysis of the simulated profiles selecting the same RoI used for the data).

The simulation of the anthropomorphic phantom set-up has not been yet performed.

3 Results

3.1 *Results of the Measurements with the Polymethyl Methacrylate Phantoms*

In this part, we report on the results obtained in the first set of measurements with the $5 \times 5 \times 14$ cm^3 PMMA phantoms. Figure 6 shows the central slice (parallel to the PET heads) reconstructed from the experimental data acquired during the interspill [Fig. 6(a)] period (about 68 s) and the in-spill [Fig. 6(b)] period (about 17 s). To reduce the image noise, a median filter was performed applying a $3 \times 3 \times 3$ sliding-kernel on the whole FoV. The in-spill image is noisier than the interspill one due to the lower statistics (the in-spill fraction is only 20% of the whole acquisition time) and the radiation induced background.

Figure 7 shows the superposition of the normalized interspill (blue line) and in-spill (green squares) 1-D profiles normalized to their maximum. The nonflat shape of both profiles along the activated area is due to the limited angular coverage of the PET scanner and to the attenuation of the photons in the PMMA. These effects have been also simulated and experimentally observed in other systems with similar geometry.[45]

Despite the higher background of the in-spill versus the interspill profile, the proximal rise and the distal fall-off edges for interspill and in-spill data are in good agreement, and a reliable activity range measurement can be performed not only during the interspill time but also during the in-spill period. This is promising for synchrotrons with improved duty cycles (reduced interspill time), where for the same dose, the total irradiation time is reduced. The same considerations also apply to cyclotron-based facilities even though further contributions to the background are expected from the energy degraders and possibly by the beam passive shaping filters.

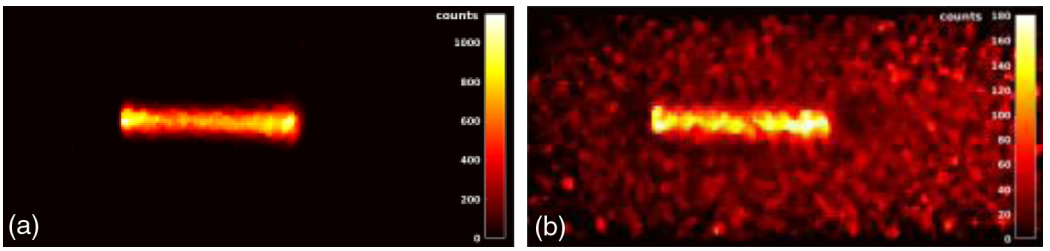

Fig. 6 (a) Interspill and (b) in-spill reconstructed events on the central slice parallel to the PET heads.

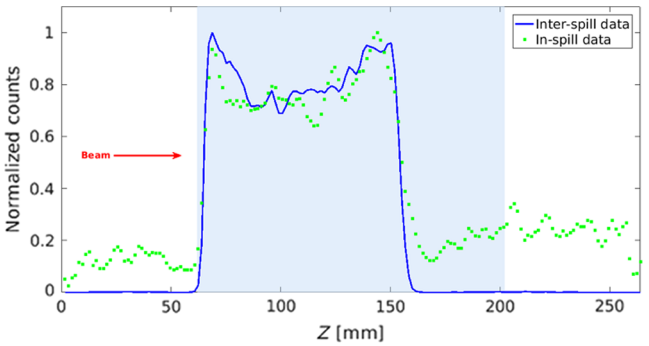

Fig. 7 Profiles normalized to the maximum of the interspill (blue line) and in-spill data (green squares). The light blue area indicates the phantom position within the FoV.

Table 2 reports the s and d parameters of the sigmoidal fit [see Eq. (1)] of the distal falloffs of the interspill and in-spill profiles, as shown in Fig. 6. The fit parameters were calculated over different left boundary values in z (the right boundary value was fixed at 200 mm), starting from $z = 65$ mm to $z = 125$ mm. We observed that, by reducing the fit interval, the goodness of the fit (R^2) improved and the confidence interval narrowed, but the fit parameters s and d were stable. Therefore, the z values used for the fit were definitely chosen between 125 and 180 mm, where the R^2 of the fit is maximum.

As can be observed, the d value for the in-spill data is comparable with the interspill one within 0.4 mm. The lower value of the slope for the in-spill profile can be explained by the contribution of the long positron range of short-lived $\beta+$ emitters,[45,46] such as ^{12}N, and the contributions of prompt photons.[16]

In the following part, we report on the results obtained for the second set of measurements with the PMMA phantoms A and B.

Figure 8 left (right) shows the central slice of the PET image of phantom A (B) obtained with a total acquisition time of 519 s (485 s). As explained in Sec. 2.4, since the Monte Carlo code considers annihilation photons arising from $\beta+$ decays only, for a realistic comparison with the simulations only interspill and after-treatment data are considered.

As shown in Fig. 6, the images were scanned with a median filter, and the integrated counts within a rectangular ROI selected on the transverse plane on each slice of the PET images were calculated.

The two energy layers are clearly visible. The higher statistics on the first layer is due to the longer integration time: in fact, the second layer has been applied 171 s after the first one in case of phantom A and 124 s in case of phantom B. Moreover, the air gap in the inhomogeneous phantom causes an overshoot of the second energy layer.

The irradiation settings described previously for the A and B phantoms were reproduced in the Monte Carlo simulation.

Figure 9 shows the normalized profiles of the simulated (continuous green line) and experimental (blue dots) images in case of phantom A [Fig. 9(a)] and phantom B [Fig. 9(b)]. The shape of the two experimental profiles in the entrance channel is different since the acquisition times are not the same for the two phantoms. The simulated and experimental profiles do not perfectly agree. For phantom A, data and simulations are in agreement at the entrance, but they do not in the dip between the two energy layers. For phantom B, the agreement is better except in the upper part of the entrance channel. To quantify the agreement in the distal part of the activity range between data and simulation in both phantoms, the sigmoidal fit has been applied to the falloffs of the activity profiles at 103.5 MeV, as shown in Fig. 9 with the results summarized in Table 3.

The slopes of the experimental data of the phantoms A and B are comparable and so are the slopes of the two simulations. However, the simulations are steeper than experimental data. This effect can be due to additional source of noise (for instance, inhomogeneity of response of the read-out channels, underestimated scattering contribution) in the experimental images not accurately modeled in simulation. Nevertheless, the inflection points of data and simulation are in agreement within 1 mm for both phantoms.

Table 2 Parameters of the sigmoidal fit of the distal falloffs of the interspill and in-spill profiles.

	s		d		
	Value	Confidence bounds (95%)	Value (mm)	Confidence bounds (95%)	Goodness of fit (R^2)
Interspill	0.68	(0.57, 0.78)	154.4	(154.2, 154.7)	0.99
In-spill	0.321	(0.295, 0.347)	154.8	(154.5, 155.0)	0.99

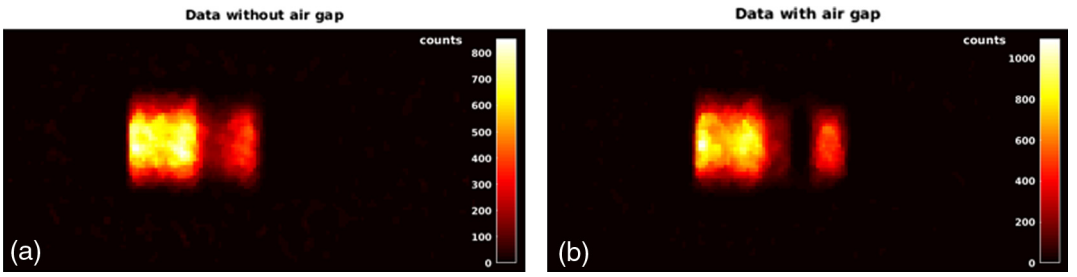

Fig. 8 (a) Image (central slice) of the phantom A obtained for an acquisition time of 519 s. (b) Image (central slice) of the phantom B obtained for an acquisition time of 485 s. In both acquisitions, only interspill and after-treatment data are considered.

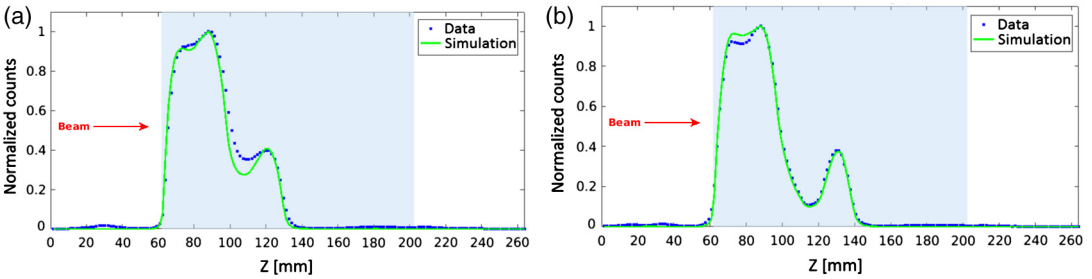

Fig. 9 Normalized profiles of the simulated (continuous green line) and experimental (blue dots) images in case of (a) phantom A and (b) phantom B.

Table 3 Results of the fit of the profiles distal falloff at 103.5 MeV shown in Fig. 9 for experimental and simulation data obtained for the irradiation on phantoms A and B, respectively.

	s		*d*		
Phantom	Value	Confidence bounds (95%)	Value (mm)	Confidence bounds (95%)	Goodness of fit (R^2)
A—Data	0.50	(0.49, 0.52)	128.9	(128.8, 129.0)	0.9992
A—Sim.	0.59	(0.57, 0.61)	128.0	(128.0, 128.1)	0.9996
B—Data	0.51	(0.47, 0.54)	137.5	(137.4, 137.6)	0.9983
B—Sim.	0.57	(0.54, 0.61)	137.3	(137.2, 137.4)	0.9988

3.2 *Results of the Measurements with the Anthropomorphic Phantom*

Figure 10 shows the image (on the coronal view) of the CT of the anthropomorphic phantom fused with the reconstructed activation map generated in the phantom by a proton beam shaped following a real treatment plan with proton energies ranging from 74 to 134 MeV. The delivered dose was 0.9 Gy (the beam enters at the right side of the image). Only interspill data are used while the after-treatment was not considered.

The aim of this test was to provide a proof of the system functionality in clinical conditions. Neither quantitative assessments of the activity range nor comparison with Monte Carlo simulations have been yet performed. Nevertheless, this result is a milestone of the INSIDE project since the PET image has been acquired and reconstructed within the irradiation session (lasting for 185 s) in a set-up reproducing a clinical treatment.

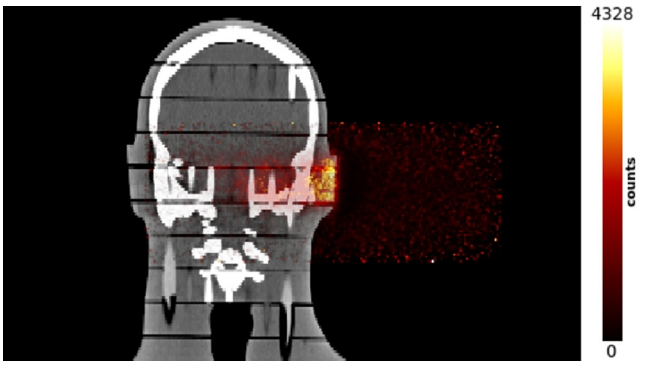

Fig. 10 Image (on the coronal view) of the CT of the anthropomorphic phantom fused with the reconstructed activation map generated in the phantom by a proton beam shaped following a real treatment plan with proton energies ranging from 74 to 134 MeV. The delivered dose was 0.9 Gy (the beam enters at the right side of the image). Only interspill data are used for the reconstruction; the after-treatment was not considered.

4 Conclusions

The INSIDE in-beam PET system described in this paper has been recently installed at CNAO and tested with proton beams. The first characterization tests have been performed with single pencil beams, energy layers, and clinical treatment plans on PMMA phantoms (both homogenous blocks and with air cavity insertions) and anthropomorphic phantoms. The beam energies (from 74 to 135 MeV) and doses (order of 1 to 2 Gy) used were compatible with those typical of treatments in the head–neck district.

The system was able to operate continuously both during the actual delivery of the beams (up to a single event count rate of 20 MHz) and during the interspill (no beam) intervals, with a CTR of about 450 ps. These performances allowed us to sort and calculate the coincidences on the fly with a time window of 2 ns. The PET images have been reconstructed with an MLEM iterative algorithm with an execution time of about 1 s on a 3.4 GHz Intel Core i7-3770 CPU. The images were divided into interspill and in-spill sets and separately analyzed.

The in-spill images show a higher noise level with respect to the interspill ones because of the lower statistics and the radiation-induced background. The contribution of short-lived isotopes and the background induced random events must be better studied in a further analysis. Nevertheless, the 1-D activity profiles show a substantial (within less than 1 mm) agreement in terms of distal falloff between the in-spill and the interspill data. This result proves the in-spill acquisition feasibility of the INSIDE PET system and its potential exploitation in a range verification protocol. At present, the CNAO synchrotron duty cycle, characterized by 1 s of spill time and 4 s of interspill, allows the acquisition of a satisfactory amount of data during the interspill intervals only. However, the duty cycle is being modified with an increase of the spill time duration (up to 3 s) and a reduction of the interspill (down to 2 s) to perform shorter treatments at the same dose. Therefore, in this scenario, the data collected during the spill will be essential.

A two-step Monte Carlo simulation taking into account the beam information provided by the CNAO DDS, the phantom, the detection system, and the reconstruction process was performed.

The comparison of the simulations and the experimental data of the activity induced in PMMA phantoms, both homogenous and with air cavities, shows an agreement in the distal fall-off position within 1 mm. Further measurements are required to assess the precision of the system. This will be done performing sets of multiple acquisitions in the same irradiation conditions at different energies and for different phantom configurations.

The next development of the INSIDE Monte Carlo code will be the production and interaction of the prompt radiation in the materials of interest (plastic phantoms and tissues) to simulate the in-spill phase.

Finally, the tests with an anthropomorphic phantom, though not quantitative, showed the capability of the system of performing the acquisition and the reconstruction of the activity induced within the irradiation session in a set-up reproducing a clinical treatment, paving the way to the clinical validation of the INSIDE in-beam PET system. Future development of the INSIDE project will be the simulation of the anthropomorphic phantom to be compared with the experimental data. This is a necessary step to assess the accuracy of the system in the measurement of the activity range in clinical conditions, and it will serve as a basis to simulate a real treatment plan starting from the patient CT.

Disclosures

The authors declare that they have no conflicts of interest.

Acknowledgments

This work was mainly supported by the Italian Ministry of University and Research (MIUR) under the program PRIN 2010-2011—INSIDE project nr. 2010P98A75. This work was also partially supported by the EU FP7-PEOPLE-2012-ITN project nr. 317446, INFIERI. The authors are very grateful to the technical staff of INFN Torino, in particular to G. Alfarone, G. Scalise (mechanical assembling of the INSIDE system), F. Dumitrache, B. Pini (hybrid microbonding), and M. Mignone and A. Zampieri (electronics). The authors wish to thank S. Giordanengo of INFN Torino for the DDS data processing and the CNAO personnel, particularly M. Ciocca, M. Ferrarini, F. Gerardi, A. Mirandola, A. Mairani, M. Pullia, A. Serra, M. Pelliccioni, and G. Baroni, S. Rossi for their kind collaboration in the installation and commissioning of the INSIDE system at CNAO.

References

1. D. Schulz-Ertner and H. Tsujii, "Particle radiation therapy using proton and heavier ion beams," *J. Clin. Oncol.* **25**(8), 953–964 (2007).
2. T. Terasawa et al., "Systematic review: charged-particle radiation therapy for cancer," *Ann. Internal Med.* **151**(8), 556 (2009).
3. A.-C. Knopf and A. Lomax, "*In vivo* proton range verification: a review," *Phys. Med. Biol.* **58**(15), R131 (2013).
4. K. Parodi, "On- and off-line monitoring of ion beam treatment," *Nucl. Instrum. Methods Phys. Res. Sect. A* **809**, 113–119 (2016).
5. A. Del Guerra, N. Belcari, and M. G. Bisogni, "Positron emission tomography: its 65 years," *La Rivista Del Nuovo Cimento* **39**(4), 155–223 (2016).
6. K. Parodi, "Vision 20/20: positron emission tomography in radiation therapy planning, delivery, and monitoring," *Med. Phys.* **42**(12), 7153–7168 (2015).
7. W. Enghardt et al., "Charged hadron tumor therapy monitoring by means of PET," *Nucl. Instrum. Methods Phys. Res. Sect. A* **525**, 284–288 (2004).
8. X. Zhu and G. El Fakhri, "Proton therapy verification with PET imaging," *Theranostics* **3**(10), 731–740 (2013).
9. X. Zhu et al., "Monitoring proton radiation therapy with in-room PET imaging," *Phys. Med. Biol.* **56**(13), 4041–4057 (2011).
10. G. Shakirin et al., "Implementation and workflow for PET monitoring of therapeutic ion irradiation: a comparison of in-beam, in-room, and off-line techniques," *Phys. Med. Biol.* **56**(5), 1281–1298 (2011).
11. T. Nishio et al., "The development and clinical use of a beam ON-LINE PET system mounted on a rotating gantry port in proton therapy," *Int. J. Radiat. Oncol. Biol. Phys.* **76**(1), 277–286 (2010).
12. B. Kozlovsky, R. J. Murphy, and R. Ramaty, "Nuclear de-excitation gamma-ray lines from accelerated particle interactions," *Astrophys. J. Suppl. Ser.* **141**(2), 523–541 (2002).
13. M. Testa et al., "Real-time monitoring of the Bragg-peak position in ion therapy by means of single photon detection," *Radiat. Environ. Biophys.* **49**(3), 337–343 (2010).
14. A. K. Biegun et al., "Time-of-flight neutron rejection to improve prompt gamma imaging for proton range verification: a simulation study," *Phys. Med. Biol.* **57**(20), 6429–6444 (2012).
15. W. Enghardt et al., "Positron emission tomography for quality assurance of cancer therapy with light ion beams," *Nucl. Phys. A* **654**(Suppl. 1), 1047c–1050c (1999).
16. G. Sportelli et al., "First full-beam PET acquisitions in proton therapy with a modular dual-head dedicated system," *Phys. Med. Biol.* **59**(1), 43–60 (2013).

17. U. Amaldi, "CNAO-the Italian centre for light-ion therapy," *Radiother. Oncol.* **73**, S191–S201 (2004).
18. A. C. Kraan et al., "Online monitoring for proton therapy: a real-time procedure using a planar PET system," *Nucl. Instrum. Methods Phys. Res. Sect. A* **786**, 120–126 (2015).
19. P. Crespo et al., "Suppression of random coincidences during in-beam PET measurements at ion beam radiotherapy facilities," *IEEE Trans. Nucl. Sci.* **52**(4), 980–987 (2005).
20. K. Parodi et al., "Random coincidences during in-beam PET measurements at microbunched therapeutic ion beams," *Nucl. Instrum. Methods Phys. Res. Sect. A* **545**(1), 446–458 (2005).
21. M. Marafini et al., "The INSIDE project: innovative solutions for in-beam dosimetry in hadrontherapy," *Acta Phys. Pol. A* **127**(5), 1465–1467 (2015).
22. G. Battistoni et al., "Measurement of charged particle yields from therapeutic beams in view of the design of an innovative hadrontherapy dose monitor," *J. Instrum.* **10**(02), C02032 (2015).
23. G. Battistoni et al., "Design of a tracking device for on-line dose monitoring in hadrontherapy," *Nucl. Instrum. Methods Phys. Res. Sect. A* (2016).
24. S. Rossi, "The status of CNAO," *Eur. Phys. J. Plus* **81**(8), 1–14 (2011).
25. F. Pennazio et al., "A study of monitoring performances with the INSIDE system," *Acta Phys. Pol. A* **127**(5), 1468–1470 (2015).
26. E. Fiorina, "An integrated system for the online monitoring of particle therapy treatment accuracy," *Nucl. Instrum. Methods Phys. Res. Sect. A* **824**, 198–201 (2016).
27. Hamamatsu Photonics, Japan, http://www.hamamatsu.com/ (July 28 2016).
28. K. Doroud et al., "Comparative timing measurements of LYSO and LFS-3 to achieve the best time resolution for ToF-PET," *Nucl. Instrum. Methods Phys. Res. Sect. A* **793**, 57–61 (2015).
29. S. Cova, G. Ripamonti, and A. Lacaita, "Avalanche semiconductor detector for single optical photons with a time resolution of 60 ps," *Nucl. Instrum. Methods Phys. Res. Sect. A* **253**(3), 482–487 (1987).
30. N. Dinu et al., "Development of the first prototypes of silicon photomultiplier (SiPM) at ITC-IRST," *Nucl. Instrum. Methods Phys. Res. Sect. A* **572**(1), 422–426 (2007).
31. N. C. Nguyen et al., "Image quality and diagnostic performance of a digital PET prototype in patients with oncologic diseases: initial experience and comparison with analog PET," *J. Nucl. Med.* **56**(9), 1378–1385 (2015).
32. G. Delso et al., "Preliminary evaluation of image quality in a new clinical ToF-PET/MR scanner," *IEEE Trans. Nucl. Sci.* **62**(3), 600–603 (2015).
33. A. Del Guerra et al., "Advantages and pitfalls of the silicon photomultiplier (SiPM) as photodetector for the next generation of PET scanners," *Nucl. Instrum. Methods Phys. Res. Sect. A* **617**(1), 223–226 (2010).
34. M. G. Bisogni and M. Morrocchi, "Development of analog solid-state photo-detectors for positron emission tomography," *Nucl. Instrum. Methods Phys. Res. Sect. A* **809**, 140–148 (2016).
35. M. A. Piliero et al., "Performance of a fast acquisition system for in-beam PET monitoring tested with clinical proton beams," *Nucl. Instrum. Methods Phys. Res. Sect. A* **804**, 163–166 (2015).
36. M. D. Rolo et al., "TOFPET ASIC for PET applications," *J. Instrum.* **8**(02), C02050 (2013).
37. B. Frisch, "Combining endoscopic ultrasound with time-of-flight PET: the EndoTOFPET-US project," *Nucl. Instrum. Methods Phys. Res. Sect. A* **732**, 577–580 (2013).
38. Y. Vardi, L. A. Shepp, and L. Kaufman, "A statistical model for positron emission tomography," *J. Am. Stat. Assoc.* **80**(389), 8–20 (1985).
39. N. Camarlinghi et al., "An in-beam PET system for monitoring ion-beam therapy: test on phantoms using clinical 62 Mev protons," *J. Instrum.* **9**(04), C04005 (2014).
40. http://www.rsdphantoms.com/rt_art.htm (27 July 2016).
41. S. Bazzano, "Status of the commissioning of the Centro Nazionale di Adroterapia Oncologica (CNAO)," in *Proc. IPAC 2010*, Kyoto, Japan, MOPEB005, pp. 283–285 (2010).
42. T. T. Böhlen et al., "The FLUKA code: developments and challenges for high energy and medical applications," *Nucl. Data Sheets* **120**, 211–214 (2014).
43. A. Ferrari et al., "FLUKA: a multi-particle transport code," CERN 2005–10, INFN/TC_05/11, SLAC-R-773 (2005).
44. S. Giordanengo et al., "The CNAO dose delivery system for modulated scanning ion beam radiotherapy," *Med. Phys.* **42**(1), 263–275 (2015).
45. A. C. Kraan et al., "Proton range monitoring with in-beam PET: Monte Carlo activity predictions and comparison with cyclotron data," *Phys. Med.* **30**(5), 559–569 (2014).
46. P. Dendooven et al., "Short-lived positron emitters in beam-on PET imaging during proton therapy," *Phys. Med. Biol.* **60**(23), 8923–8947 (2015).

Maria Giuseppina Bisogni is a professor of medical physics at the University of Pisa (Italy). She earned her PhD in physics in 1998, and she has been a specialist in medical physics since 1999. Her research activity is mainly focused on solid-state detectors and their applications to medical imaging. The most important result obtained has been the development of innovative detection modules for positron emission tomography based on silicon photomultipliers. She is a principal investigator of the INSIDE project.

Andrea Attili was a PhD candidate at the Università degli Studi "Roma Tre," Roma (Italy), in condensed matter physics (glasses and supercooled liquids) from 2000 to 2003. From 2004 to 2005, his research activity was in bioinformatics (proteins tertiary structure modeling) at the Department of Biochemical Sciences, Università "La Sapienza," Roma. From 2006, he has been doing research in medical physics (radiobiological models and planning for ion beam radiotherapy) at INFN (Istituto Nazionale di Fisica Nucleare), Sezione di Torino (Italy).

Giuseppe Battistoni has been an INFN researcher since 1982. He participated in experiments in particle and nuclear physics with accelerators, in cosmic ray physics and neutrino physics, working on the development of particle detectors and Monte Carlo simulation. Since 2006, he has mainly worked on the application of nuclear and particle physics to medicine, contributing to the research in hadrontherapy. In particular, he contributed to the work for new treatment planning systems and to the development of *in-vivo* monitoring techniques.

Nicola Belcari received his PhD in applied physics from the University of Pisa in 2003. Since 2007, he has been a researcher in the Department of Physics of the University of Pisa, and since 2010, he has been a staff assistant professor. His present research is oriented on the development of multimodality instrumentation for high-resolution preclinical PET/CT and brain-dedicated PET/MRI systems. He is also an expert on performance assessment of preclinical PET/CT instrumentation.

Niccolo' Camarlinghi obtained his PhD in applied physics in 2002 at University of Pisa (Italy). He is currently working as a researcher at Pisa University (Italy) in the field of positron emission tomography (PET).

Piergiorgio Cerello earned his PhD in nuclear physics in 1995. Among the founders of the CERN/ALICE project, from the early 2000s, he developed an interest in medical applications, initially working on computer-assisted-detection algorithms for the identification of lung nodules in CT. He is now involved in the construction of a PET/MR/EEG scanner for the study of schizophrenia as well as on the INSIDE project for range monitoring in particle therapy.

Silvia Coli graduated in aerospace engineering at Politecnico of Turin. She has been a technologist at INFN (TURIN section) since 2000 (permanent position since 2008). Her principal research and experimental activities include the responsibility for the cooling system project and expert on call of the ALICE-ITS, responsibility for the cooling system project of PANDA-MVD, and responsibility for the development of the stave assembly procedure in all the production sites of the ALICE UPGRADE-ITS-OB.

Alberto Del Guerra is now a retired professor of medical physics at the University of Pisa (Italy). Previous appointments were professor of medical physics (University of Ferrara), professor of physics (University of Napoli), visiting scientist at LBL (Berkeley), visiting professor at UW (Seattle), and president of EFOMP. He is an IEEE fellow and honorary editor of *Physica Medica*. His main research interests are in medical imaging, especially PET, with more than 350 papers in refereed journals.

Veronica Ferrero graduated in physics in 2014 at the University of Torino (Italy) with a thesis focused on the radiobiological effects of gold nanoparticles in radiotherapy. She is currently doing her PhD on the INSIDE project.

Elisa Fiorina graduated in physics in 2009 and obtained her PhD in physics in 2013 at the University of Torino with a thesis on the development of algorithms for medical image processing and segmentation. Since 2013, her research activity is carried out in the INSIDE Project, focused on the development of Monte Carlo simulations for in-beam PET, implementation of data acquisition systems, and data analysis.

Giuseppe Giraudo received the degree in physics at the Università of Torino in 1992. He is currently as senior technologist at INFN Torino. Among the latest experimental activities, he is supervisor of the mechanical structure and system integration of ITS Alice at CERN LHC, MVD Panda at GSI-FAIR and INSIDE In Beam PET at CNAO. He is a supervisor of the mechanical design bureau of INFN Torino 2004 to 2016. Also, he is a advisor/member of the technical board of Panda Project at GSI-FAIR.

Eleftheria Kostara studied physics at Aristotle University of Thessaloniki. In 2013, she obtained an MSc degree in electronic physics (radioelectrology) in the same university with a master's thesis on FPGA implementation of a real-time video processing system. Currently, she is a PhD student at University of Siena and a Marie Curie Fellow within the INFIERI network with a concentration in medical physics at INFN in Pisa. She is interested in data acquisition systems for full-beam PET in hadrontherapy.

Matteo Morrocchi is currently a postdoc researcher in the Department of Physics at the University of Pisa. He is currently collaborating on the TRIMAGE project, working on the development of the positron emission tomography scanner. He received his PhD in physics in 2015 at the University of Pisa, using pixelated and monolithic scintillators coupled to silicon photo-multiplier arrays to develop high spatial resolution PET detectors, which is his main research interest.

Francesco Pennazio graduated in medical physics in 2008 and obtained his PhD in physics in 2013 at the University of Torino. His research activity focuses on Monte Carlo simulations and experimental data analysis of PET and in-beam PET systems.

Maria Antonietta Piliero has recently finished the medical physics clinical training at the University of Pisa and is currently working at the Medical Physics Department at the Santa Chiara Hospital, Pisa, Italy. In 2013, she received her PhD in medical physics from Swansea University, Wales, United Kingdom, sponsored by the Cancer Research Wales. His research interests include dosimetry in the radiotherapy and nuclear medicine fields.

Giovanni Pirrone started studying medical physics at the university of Pisa (Italy) and received his MSc degree in January 2013. In April 2013, he joined as a research fellow the INSIDE collaboration, a project that addresses the online monitoring in particle therapy. From 2013, he also attended the Specialty School in Medical Physics of Pisa and specialized in September 2016.

Valeria Rosso earned her degree in physics and PhD at Specialty School in Health Physics at University of Pisa. She is a professor at Physics Department "E. Fermi" and director of Specialty School in Health Physics, University of Pisa. She has been involved in medical physics research, particularly in the development of imaging detectors and techniques, mainly for digital radiography and for the quality assurance in particle therapy. She has been and is scientific coordinator of research projects supported by INFN.

Paola Sala earned her degree in physics in 1984 and the PhD in 1991 with activity mainly devoted to nuclear structure studies based on gamma ray spectroscopy. Since 1991, she has been a member of the ATLAS collaboration and then was involved in neutrino observation experiments. She is one of the main developers of the FLUKA Monte Carlo code.

Giancarlo Sportelli studied electronics engineering at the Italian Polytechnic of Bari. In 2010, he obtained his PhD degree at the Telecommunications Engineering School of the Universidad Politécnica de Madrid. In 2011, he joined the Functional Imaging and Instrumentation Group as an INFN postdoc fellow. He worked on high-performance PET data acquisition architectures, full-beam PET in hadron therapy, and SiPM based PET. Now, he is a researcher of the group working on PET/MR instrumentation.

Richard Wheadon received both his degree and doctorate in physics from Imperial College, London. He is a technology researcher for INFN Turin, Italy with more than 25 years of experience in the field of silicon sensor applications for both high energy physics and medical imaging. He has been working for the INFN since 1994 on both sensor R&D and apparatus design, prototyping, and construction.

Biographies for the other authors are not available.